
Reduction of the Ablative Rayleigh–Taylor Growth Rate with Gaussian Picket Pulses

Introduction

The compression of an inertial confinement fusion (ICF)¹ target must achieve high hot-spot temperatures ($T \gtrsim 10$ keV) and shell areal densities ($\rho R \gtrsim 300$ mg/cm²) to ignite. An ICF implosion is subject to the Rayleigh–Taylor (RT)^{2,3} instability as the shell accelerates inward and as the shell decelerates toward stagnation, causing small perturbations in the shell of the target to grow, potentially reducing the ultimate temperatures and areal densities. This instability can be mitigated two ways: reduction of the seed perturbation amplitudes and reduction of the RT growth rate. Much effort has gone into reducing the seeds of the RT instability due to the roughness of the inner and outer surfaces of the shell, as well as increasing the uniformity of the laser illumination or driving radiation. In this article, we report on the first observations of reduced RT growth rate using a prepulse or *picket* pulse^{4,5} preceding a main laser-drive pulse in planar-target experiments.

Laser ablation provides the pressure needed to implode an ICF target. For large ablation velocities and short wavelengths, ablation eliminates the RT growth because the tips of the perturbation on the outer surface of the shell ablate more quickly than the troughs of the perturbation. This is reflected in the growth rate γ of an interface bearing a spatial perturbation with wave number k , approximated by the generalized dispersion formula^{6–8}

$$\gamma = \alpha \sqrt{\frac{kg}{1+kL}} - \beta k V_a, \quad (1)$$

where g is the acceleration, V_a is the ablation velocity, and L is the density scale length, $|\partial \ln \rho / \partial z|^{-1}$, at the ablation surface. The fitting constants for polystyrene (CH) are given by $\alpha = 0.98$ and $\beta = 1.7$ (Ref. 8). The ablation velocity is given by $V_a = \dot{m}/\rho_a$, where \dot{m} is the rate of mass ablation per unit area determined by the illumination intensity and ρ_a is the density of the material just before ablation.

The RT instability is completely stabilized for all wavelengths less than some “cutoff” wavelength λ_c , which is determined by setting γ equal to 0, from Eq. (1):

$$\lambda_c = 4\pi L \left(\sqrt{1 + \frac{4\alpha^2}{\beta^2} \frac{gL}{V_a^2}} - 1 \right)^{-1}. \quad (2)$$

For example, if $g \sim 10^{16}$ cm/s² (100 μm/ns²), $V_a \sim 2$ μm/ns, and $L \sim 1$ μm, then the cutoff wavelength is given by $\lambda_c \sim 3$ μm. From Eq. (2) we see that $\lambda_c \propto V_a$ if $V_a^2 \ll gL$. By using the definition of V_a , we see that $\lambda_c \propto 1/\rho_a$. A decrease of ρ_a by a factor of 3 for the same acceleration and scale length raises the cutoff wavelength to $\lambda_c \sim 10$ μm. This may be accomplished by irradiating the target with an intense picket pulse, followed by a relaxation period before the onset of the main drive pulse.

In this scheme, the picket pulse sends a shock wave through the target, heating it. The target expands during the period of relaxation after the picket. A sufficient relaxation period allows the ablator to expand to less than solid density. As a result of the relaxation-phase expansion, the ablation velocity during the drive pulse will be greater than without the picket pulse, and the RT growth rate will be decreased.⁹

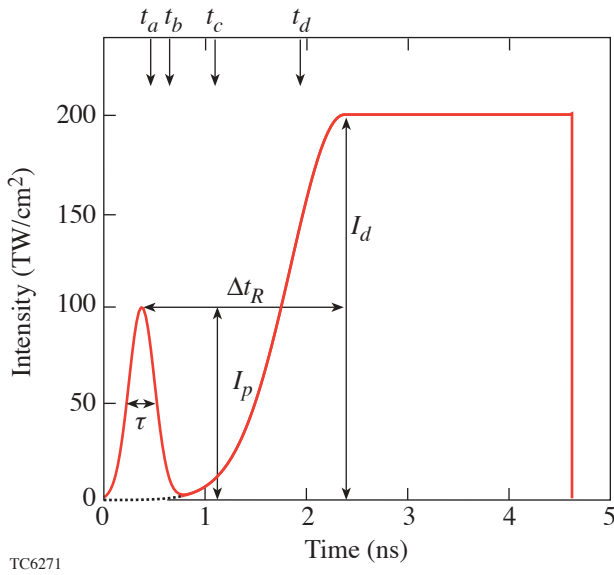
In addition to growth-rate reduction, pickets are predicted to reduce laser-induced imprint.¹⁰ The standoff distance between the critical surface and the ablation surface determines the degree to which the laser illumination perturbations are imprinted on the target.¹¹ The increased intensity of the picket results in a greater growth of the standoff distance at the start of the pulse. This benefit must be balanced—when smoothing techniques such as smoothing by spectral dispersion (SSD)¹² are used—against the loss of smoothing time when the conduction zone grows more quickly. In the experiments described here, the initial mass modulations are chosen to be large enough that laser imprint amplitudes are not significant.

We report here on direct-drive planar-target experiments with the OMEGA laser system¹³ where planar targets are used to study at the ablation surface during the acceleration phase.¹⁴ Planar geometry allows the use of through-foil x-ray radiography to determine the growth of the optical-depth modulation of an initially mass-modulated target, providing a measure of the areal-density growth. In these experiments, the planar target has a surface modulation on the side illuminated by the drive laser beams. While the target is driven, it is subject to the ablative RT instability. Analysis of the optical-depth modulation allows the determination of the RT growth rate. The fundamental Fourier-mode amplitudes of the measured optical-depth modulations will be compared with those determined from 2-D simulations, demonstrating reduction of the RT growth rate through the use of shaped pulses employing a single picket pulse.

In the following sections, (1) the design of the picket pulse using 1-D simulations will be described; (2) the experiment will be described in detail; and (3) experimental results will be compared to the results of 2-D simulations and discussed.

Unperturbed Planar Hydrodynamics

The laser pulses shown in Fig. 95.1 with (solid line) and without (dotted line) a picket pulse were simulated to investigate the effects of a picket pulse in planar geometry and to determine the optimal pulse shape for this experiment. The drive portion of the pulses is identical, so the only difference between the two pulses is seen in the temporal region of the picket pulse. The pulse shape with the picket pulse consists of a Gaussian picket pulse with an intensity I_p and width τ ,



TC6271

followed by a period of relaxation Δt_R , and then by a drive pulse with a Gaussian rise to a period of constant intensity I_d . The evolution of a planar, 20- μm -thick CH foil driven by this laser pulse was computed with the 1-D hydrodynamic simulation code *LILAC*.¹⁵ The effects of the laser pulse can be determined by studying the spatial profile of the inverse of the pressure scale length $L_p^{-1} \equiv |\partial \ln p / \partial z|$ as a function of time [Fig. 95.2(a)]. The pressure scale length has local minima where the pressure gradient is largest. This allows shock-wave and rarefaction-wave boundaries to be identified. The mass-density profile of the foil is shown in Fig. 95.2(b) for four times: t_a , t_b , t_c , and t_d , which are also labeled in Figs. 95.1 and 95.2(a). These times represent four stages in the evolution of the foil:

Stage 1 (t_a): The picket pulse launches a shock wave (SW) into the target. At time $t_a \sim \tau$, the picket pulse ends and the pressure supporting the SW drops quickly. This drop in pressure is communicated to the target as a rarefaction wave (RW) sent into the target. The leading edge of this RW catches up to the shock wave at the sound speed of the shocked material. The RW also causes the front surface of the target to expand outward.

Stage 2 (t_b): Shortly after $t \sim t_b$, the SW reaches the rear surface of the foil. For this foil thickness, t_b is comparable to the time when the leading edge of the first RW overtakes the picket-pulse shock wave. The shock wave's breakout time is given by $t_b = d/D$, where d is the width of the foil and D is the picket shock speed.

Figure 95.1

The analytical pulse shapes used to design the planar picket-pulse experiments. The picket pulse (shown as the solid line) is a Gaussian pulse, as is the rise to the main “drive” pulse. The intensity I_p of the picket pulse is 100 TW/cm², half the intensity I_d (200 TW/cm²) of the drive pulse. The half-width $\tau/2$ at half maximum intensity of the picket pulse is 150 ps and of the Gaussian rise for the drive pulse is 750 ps. The time Δt_R from the peak of the prepulse to the maximum of the drive pulse is 2 ns. The pulse without the picket is shown as a dotted line. The drive pulse with and without the picket is identical, and the only difference is in the temporal region of the picket pulse.

Stage 3 (t_c): Once the picket-pulse shock wave reaches the rear side of the foil, a second RW is sent back from the rear toward the front of the target, potentially passing through the first (end-of-picket) RW. The picket pulse is followed by a

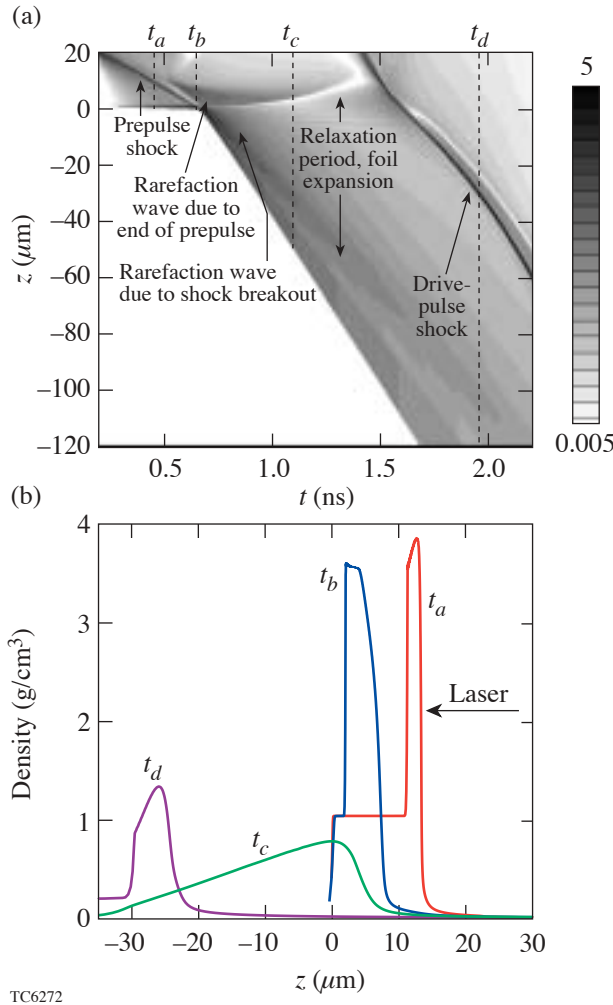


Figure 95.2

(a) A space-time diagram of a 20- μm -thick plastic target driven by the picket pulse shown in Fig. 95.1. The quantity plotted is the inverse of the pressure scale length $|\partial \ln p / \partial z| (\mu\text{m}^{-1})$, which has local maxima where the pressure gradient is largest, allowing shocks and rarefaction-wave boundaries to be identified. Vertical dashed lines are drawn at the times of the density plots in Fig. 95.2(b). The behavior shown is qualitatively the same as for the Gaussian picket pulse; a square picket pulse is used instead to clarify the RW boundaries. (b) The density profile at various times during the evolution of a 20- μm foil driven by the prepulse shape of Fig. 95.1 but with a square picket. The profiles shown are at 0.46 ns (t_a), during the picket pulse; 0.65 ns (t_b), after the picket pulse has ceased but before shock wave breaks out; 1.1 ns (t_c), during the relaxation period while the foil is expanding; and 1.96 ns (t_d), after the drive pulse has begun to sweep up the foil, driving a shock through it.

relaxation period Δt_R during which the foil expands approximately adiabatically for low-Z materials. If the shock wave breaks out of the foil before the drive pulse begins, the front surface of the foil expands due to the passage of two RW's. This is shown at time t_c in Fig. 95.2(b). Otherwise only the front surface will expand as the picket-pulse RW propagates into the target. If the edges of the foil expand at constant speed, the average density is approximately inversely proportional to time. The spatial peak density of the foil, using *LILAC*, is shown in Fig. 95.3(a) without the picket pulse (solid line) and with the picket pulse (dotted line).

Stage 4 (t_d): At time t_d , the drive pulse reaches its peak. The drive pulse launches one or more shock or compression waves into the target. The density profile of the foil as these shocks are launched depends on the duration of the expansion period, given approximately by $t \sim \Delta t_a - \tau/2$. The density profile, in turn, determines the density of the ablated material, the ablation velocity [see Fig. 95.3(b)], and the degree of ablative RT stabilization during the acceleration of the foil. The density scale length L , acceleration, and RT growth rate are also shown in Figs. 95.3(c)–95.3(e) for a Gaussian-rise drive pulse with (solid line) and without (dotted line) a picket pulse. The thermal relaxation time after the picket pulse and the effects of absorption of x rays from the corona plasma result in a density scale length that is increased by a factor of 2 during the drive pulse over the scale lengths without the picket. This is large enough to change the scale-length RT growth mitigation term $(1 + kL)$ from 1.3 to 1.6 for a 20- μm -wavelength perturbation. The ablation velocity is a factor of 3 to 4 larger for pulse shapes with a picket pulse than without a picket pulse, providing an even larger reduction in the growth rate [see Fig. 95.3(e)].

The intensity I_p and duration τ of the picket pulse and the length of the relaxation period Δt_R in this experiment satisfy the following constraints: (1) The picket-pulse energy is much smaller than the drive-pulse energy. (2) The duration of the pulse, including the picket pulse, is shorter than the time it takes a sound wave to cross the laser spot (which has a diameter of 600 μm at 90% intensity), allowing the shock front to remain planar, which, in turn, allows for the accurate measurement of perturbation growth with through-foil radiography. (3) The relaxation period is chosen to preclude the optical depth of the foil dropping below the sensitivity of the x-ray backscatter before being recompressed by the drive pulse.

The time-averaged ablative RT growth rate $\langle \gamma \rangle$ for a 20- μm -wavelength surface perturbation averaged over 2 ns after the start of the drive pulse is plotted in Fig. 95.4 as a

function of the three parameters: I_p [Fig. 95.4(a)], $\tau/2$ [Fig. 95.4(b)], and Δt_R [Fig. 95.4(c)]. The nominal picket parameters for this study are $I_p = 100 \text{ TW/cm}^2$, $\tau = 300 \text{ ps}$, and $\Delta t_R = 2 \text{ ns}$. Two of these values were held constant while varying the third. Figures 95.4(a) and 95.4(c) show that the average growth rate during the drive pulse is inversely dependent on the picket-pulse intensity and the relaxation time. This inverse dependence demonstrates that the main effect of the picket is to deposit sufficient energy to decompress the target. The average growth rate initially decreases with increasing picket width because the greater energy delivered by the picket

results in greater decompression of the foil. For widths greater than $\sim 150 \text{ ps}$, however, the relaxation time is insufficient to allow decompression (recall that the relation time Δt_R is given by the peak-to-peak time, which is reduced by the half-width of the picket), and the average growth rate then increases with τ . The drive pulse consisted of a 750-ps Gaussian rise to a 200-TW/cm² flattop pulse. The picket intensity was varied during the experiment, and its effect on the ablative stabilization of RT growth was observed.

Experimental Configuration

A schematic of the experimental layout (Fig. 95.5) shows the orientation of the three foils and diagnostics used in this experiment.¹⁴ The laser drive beams were incident onto the CH-foil drive target, which was mounted on a Mylar washer with a 1-mm hole in the center. A 2-mm \times 2-mm piece of 25- μm -thick uranium was mounted 9 mm from the drive foil. The backlighter beams irradiated the uranium foil in order to generate the x rays needed to radiograph the accelerated foil. A third foil (6- μm -thick aluminum) centered between the drive and backlighter foils acted as a bandpass filter for

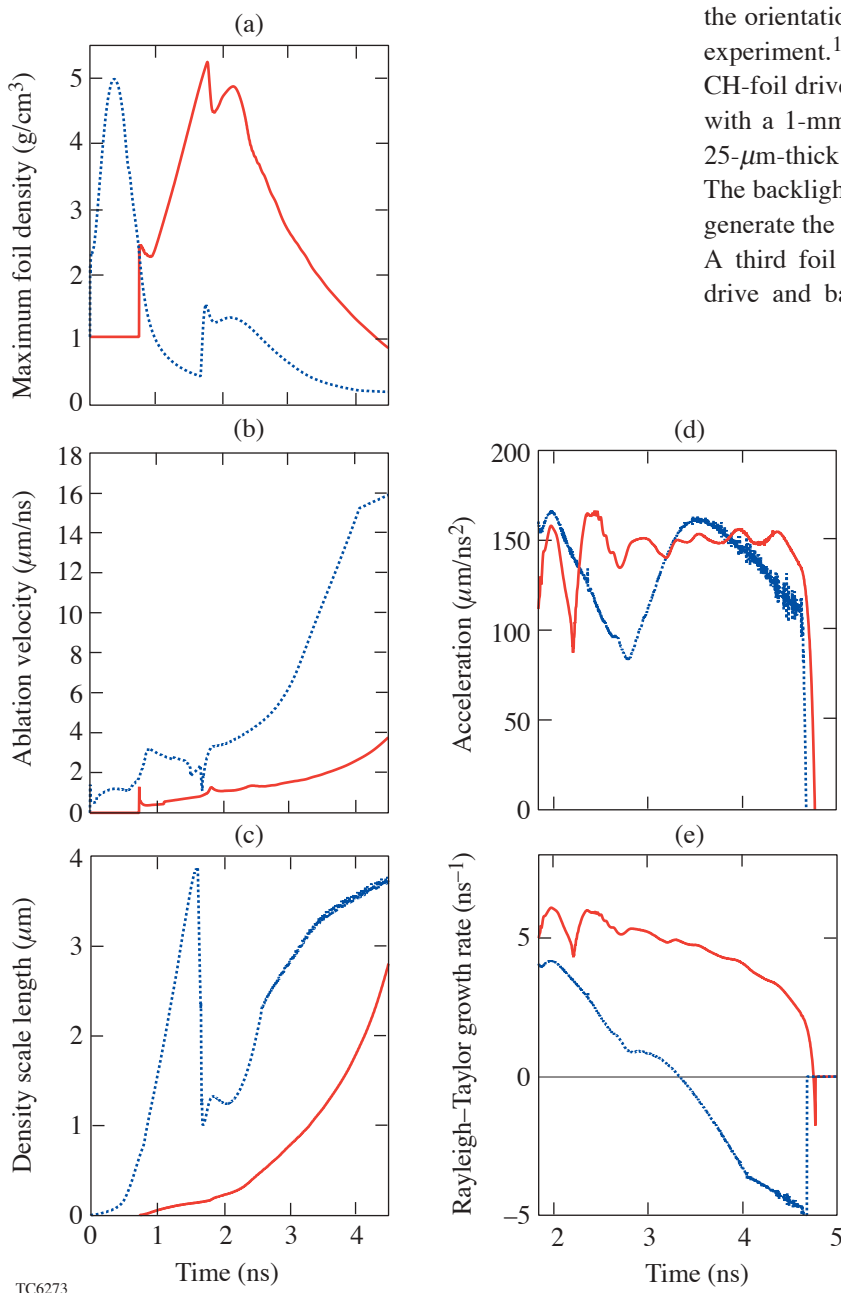


Figure 95.3
 (a) The peak foil density, (b) ablation velocity, (c) density scale length at the ablation surface, (d) shell acceleration (found by differentiating twice the centroid position), and (e) the Rayleigh-Taylor growth rate [Eq. (1)] for a 20- μm perturbation are shown as functions of time as computed from 1-D LILAC simulations using the analytic Gaussian picket-pulse shape (dotted) and a bare drive pulse (solid). The growth rate is set to zero for imaginary values. The peak density is as much as a factor of 6 lower for the picket-pulse shape than that for the non-picket drive. The resulting ablation velocity during the drive pulse with the picket pulse is as much as a factor of 6 greater than that of the drive pulse without the picket pulse. The ablation-interface density scale length is two to three times larger for the drive pulse that includes the picket pulse. The acceleration during the target drive is comparable for both pulses. The growth rate calculated from Eq. (1) is significantly smaller when the picket pulse is added to the drive.

x rays between 1.0 and 1.5 keV. This prevented the very-low-energy x rays from the uranium target from preheating the accelerated foil.

The mass-modulated accelerated foil was composed of a 20- μm -thick CH foil with perturbations imposed on the side irradiated by the laser. This thickness was chosen because it has about two attenuation depths for the 1.0- to 1.5-keV x rays used for radiography. The spectrally and response-weighted mean free path for x rays emitted from the backlighter target is 12 μm . The initial perturbations were (1) a wavelength of $\lambda = 60 \mu\text{m}$ and amplitude of $a = 0.025 \mu\text{m}$; (2) $\lambda = 30 \mu\text{m}$ and $a = 0.125$ and $0.25 \mu\text{m}$; and (3) $\lambda = 20 \mu\text{m}$ and $a = 0.05$ and $0.25 \mu\text{m}$. The perturbation amplitudes decreased with decreasing wavelength to ensure that the growth was measured in the “linear” ($a < \lambda/10$) regime of the RT instability. The 0.25- μm -amplitude perturbation at wavelengths of 30 μm and 20 μm was used to study the stability of this perturbation for large picket intensities where little or no growth was expected and the smaller-amplitude perturbation was below the detection threshold.

The primary diagnostic for the amplitude-growth measurements was an x-ray framing camera.¹⁶ The pinhole array was composed of eight 8- μm -diam pinholes arranged in a checkerboard pattern to minimize interference from adjacent images. The framing camera had a magnification of 14.1 ± 0.1 . The noise levels on the framing camera allow the instrument to measure perturbations with amplitudes greater than 0.2 μm . As a result, the early-time amplitudes of the accelerated foils were below the detection limit. The modulation transfer function for the x-ray framing camera was measured prior to the experiment and has values of 0.87, 0.65, and 0.42 at spatial periods of 60, 30, and 20 μm . These values were used to compare the hydrodynamic simulations of the optical depth to the experimental measurements.

A second x-ray framing camera measured the spatial and temporal emissions of the backlighter at a magnification of 6 with a standard 16-pinhole array where each pinhole was 10 μm in diameter. This diagnostic was used to monitor the temporal and spatial x-ray emission from the uranium backlighter. It was filtered to be sensitive to the same x-ray

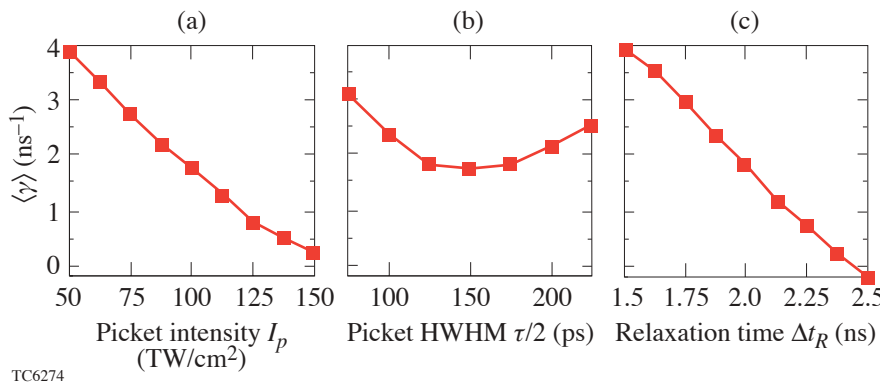


Figure 95.4

The dependence of the average ablative RT growth rate $\langle \gamma \rangle$, as determined from LILAC simulations, on picket parameters (see Fig. 95.1): (a) the picket-pulse intensity I_p , (b) duration (HWHM) $\tau/2$, and (c) the relaxation time Δt_R (given by the time from the peak of the picket pulse to the peak of the drive pulse). These variations were used to identify the optimal picket for the experiment. The growth rate is averaged over 2 ns starting from the launch of the drive-pulse shock.

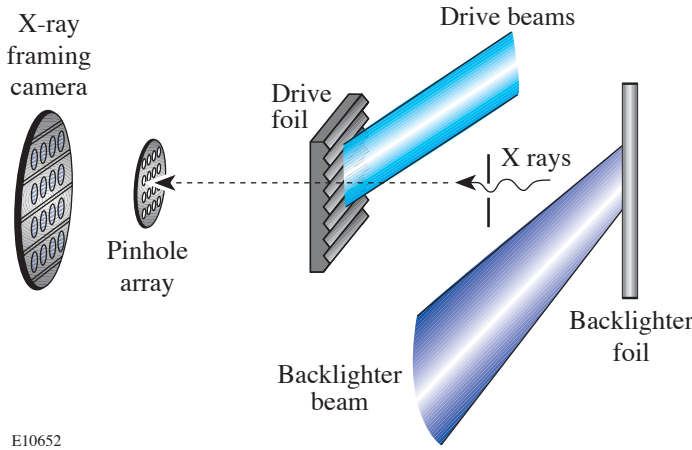


Figure 95.5

Experimental schematic of the target and primary diagnostic. The target is constructed from three foils: a uranium backlighter, an aluminum debris shield, and a CH drive foil with an imposed perturbation. The backlighter foil is 9 mm away from the drive foil with the Al shield halfway between these targets. The primary diagnostic is an x-ray framing camera with a 14.1 magnification provided by 8- μm pinholes located 24.8 mm from the accelerated target.

spectrum incident on the drive target. These data were used to determine the spatial shape of the x-ray backscatter so that it could be subtracted from the radiograph.

The time for each radiograph recorded by the framing cameras was determined by measuring when each strip on the framing camera was active and where the image was on the strip. The timing accuracy of each image relative to the drive beams was about 100 ps. The temporal resolution of both x-ray framing cameras was 80 ps.

Laser Irradiation

Planar-foil experiments on the OMEGA laser system use two independent laser sources so that separate pulse shapes can be used for the drive and backscatter beams. The beams were overlapped onto their respective targets with a radial displacement accuracy of 35 μm from the center of each foil. The backscatter pulse shape used was a 2-ns-duration square pulse. Each backscatter beam was focused to a 2.0-mm-diam spot at the 5% intensity contour with a maximum intensity where the beams overlapped on the foil of $2.0 \times 10^{14} \text{ W/cm}^2$. Planar targets with imposed mass perturbations were accelerated using ten laser beams overlapped with a total overlapped peak intensity of $1.7 \times 10^{14} \text{ W/cm}^2$. Each of the drive beams was focused to a spot size with a diameter of $\sim 930 \mu\text{m}$ (at the 5% intensity contour) and incorporated all of the beam smoothing available on OMEGA. The use of distributed phase plates,¹⁷ polarization smoothing,¹⁸ and SSD¹² resulted in a laser-irradiation nonuniformity relative to the intensity envelope of $<1\%$ over a 600- μm -diam region defined by the 90% intensity contour. Two pulse shapes were used for the drive beams: first, a pulse with a Gaussian rise to a 2-ns constant intensity (referred to as the drive pulse) and, second, this same pulse with a Gaussian picket placed ~ 2 ns ahead of the time when the drive pulse reaches constant intensity. The generic pulse shapes are shown in Fig. 95.1. The maximum drive intensity was designed to be the same for irradiation with and without a picket; however, for all data, the drive intensity with the picket was $\sim 10\%$ lower than that without the picket. To produce a clearly measurable result, the picket-pulse intensities used are greater than would be used to drive an actual ICF target.

Two-Dimensional (2-D) Simulations and Comparison with Experimental Results

Two-dimensional (2-D) hydrodynamic simulations of the experiments were performed with the Arbitrary-Lagrangian-Eulerian hydrodynamics code DRACO.¹⁹ These simulations

included flux-limited thermal diffusion, diffusive multigroup radiative transport (four groups were found to be sufficient), and inverse-Bremsstrahlung laser-energy deposition modeled with a straight-line ray trace. The experimentally measured pulse shape for a characteristic shot from each series (wavelength and picket intensity) was used. The Fourier transform of the optical-depth modulation of these simulations was calculated, incorporating the uranium backscatter spectrum, the filtering of the x-ray framing camera, and a correction for the camera resolution.

A comparison of the calculated and measured amplitudes of the fundamental Fourier mode of the optical-depth modulation is shown in Fig. 95.6 for a drive pulse only, a picket 50% of the drive-pulse intensity, and a picket 100% of the drive intensity. The data with and without the picket have been synchronized to the start of the measured drive pulse. Multiple shots were performed for each wavelength, with the x-ray diagnostics using a different temporal window for each shot. This allowed coverage over much of the duration of the drive pulse. There is no measured or calculated difference in the RT growth for perturbation wavelengths of 60 and 30 μm for a picket-pulse intensity of 50% of the drive pulse [Figs. 95.6(a) and 95.6(b), solid and dotted lines]. By contrast, a clear reduction in the growth rate is seen for the 50% picket data for the 20- μm -wavelength perturbation [Fig. 95.6(c), solid line]. Data for a picket with an intensity of 100% of the drive pulse [Figs. 95.6(b) and 95.6(c), dashed lines] show that the growth is clearly less for both 30- μm - and 20- μm -wavelength perturbations, and in fact, the ablation velocity during the drive pulse is large enough to stabilize the RT growth at these wavelengths. Two-dimensional hydrodynamic simulations of the experiment agree with the experimental data without and with picket pulses.

The dependence of the averaged 20- μm -wavelength RT growth rate on the picket intensity is shown in Fig. 95.7. The growth rate is calculated by fitting the experimental modulation in optical-depth data with an exponential for the pulse shapes with a picket pulse: $I_p/I_d = 50\%$ and $I_p/I_d = 100\%$. These data are plotted as solid points with error bars. The error bars are the statistical errors calculated from the exponential fit. The experimental points are compared to the LILAC data from Fig. 95.4(a) plotted as open circles. The picket intensity from Fig. 95.4(a) is divided by 200 TW/cm^2 to determine I_p/I_d . The average RT growth rates calculated by LILAC agree with the experimental data.

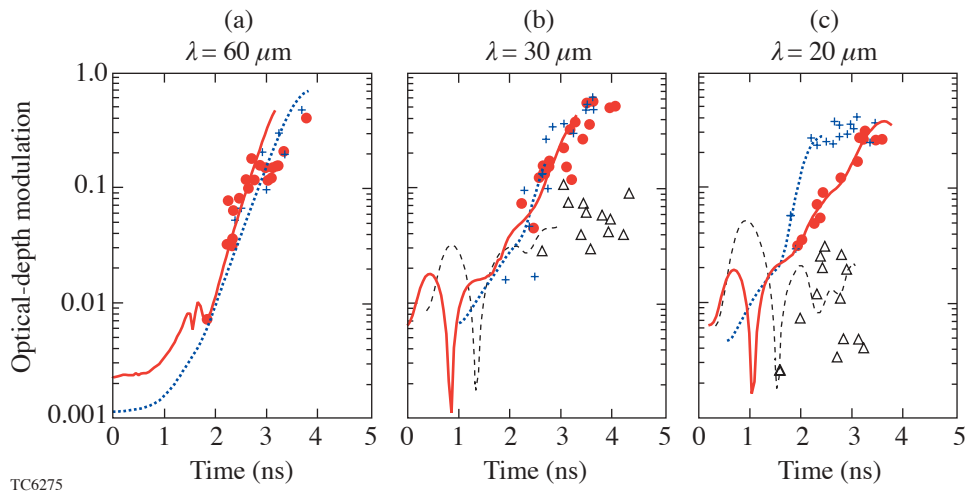


Figure 95.6

The optical-depth modulation for (a) 60- μm -, (b) 30- μm -, and (c) 20- μm -wavelength perturbations for laser pulse shapes without a picket pulse, with a picket-pulse intensity approximately 50% of the drive pulse, and with a picket-pulse intensity approximately 100% of the drive pulse. The *DRACO* 2-D hydrodynamic simulation data are shown using curves and the experimental data as symbols. *DRACO* output for a no-picket pulse is plotted as a dotted line, and experimental data for no picket are plotted as crosses. Laser pulse shapes with a picket intensity of about 50% of the drive intensity have the *DRACO* output plotted as a solid line and the experimental data as circles. A picket pulse with an intensity of about 100% of the drive intensity is shown as a dashed line for the *DRACO* output, and the experimental points are plotted as open triangles.

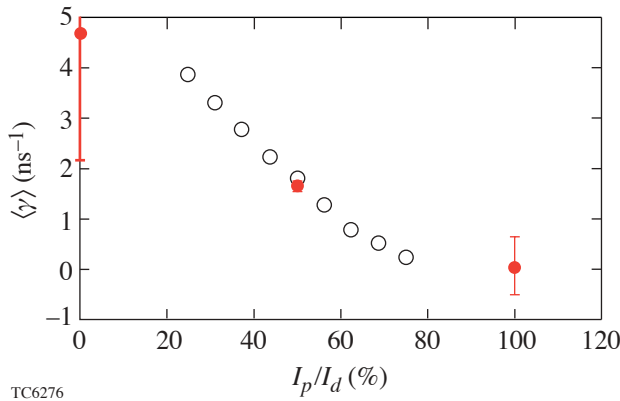


Figure 95.7

The average growth rate for a 20- μm -wavelength perturbation is plotted as a function of the picket-pulse intensity (I_p) divided by the drive-pulse intensity (I_d). The solid points are calculated by fitting the experimental data to an exponential. The error bars on the experimental points reflect the statistical error from the exponential fit. The open circles are the *LILAC* points from Fig. 95.4(a) replotted as a comparison to the measurements.

Conclusions

Experiments have been performed on the OMEGA laser system to test the reduction of the RT growth rate using a single laser picket before the main drive pulse. One-dimensional (1-D) hydrodynamic simulations used to define the experimental parameters indicate that a picket pulse with an intensity of 100 TW/cm² and a FWHM of 300 ps and separated from the drive pulse by 2 ns showed significant reduction in the RT growth rate for a 20- μm -wavelength perturbation. The picket generates a shock wave in the foil, allowing it to expand and

rarefy during the relaxation period. As a result, the foil density during the drive pulse is lowered, and the ablation velocity is correspondingly higher, lowering the RT growth rate. This has been observed experimentally in planar targets in which the RT growth rate was determined by optical-depth modulations measured with x-ray backlighting.

With a picket-pulse intensity equal to 50% of the drive-pulse intensity, the RT growth was reduced for a 20- μm -wavelength surface perturbation, but negligible growth

reduction was observed for perturbation wavelengths of 30 and 60 μm . RT growth data taken with a picket-pulse intensity equal to 100% of the drive-pulse intensity show that both the 30- and 20- μm -wavelength perturbations exhibit no significant RT growth. The modulation in optical depth as a function of time calculated from 2-D hydrodynamic simulations agrees with the experimental data.

The dependence of the time-averaged RT growth rate on the picket intensity for the 20- μm -wavelength perturbations was calculated from the experimental data. These data were then compared to the time-averaged RT growth rates calculated by *LILAC* when the experiment was designed. The ablative RT growth rate's dependence on the intensity of the picket calculated by *LILAC* agrees with the experimental data.

ACKNOWLEDGMENT

This work was supported by the U.S. Department of Energy Office of Inertial Confinement Fusion under Cooperative Agreement No. DE-FC03-92SF19460, the University of Rochester, and the New York State Energy Research and Development Authority. The support of DOE does not constitute an endorsement by DOE of the views expressed in this article.

REFERENCES

1. J. Nuckolls *et al.*, *Nature* **239**, 139 (1972).
2. Lord Rayleigh, *Proc. London Math Soc.* **XIV**, 170 (1883).
3. G. Taylor, *Proc. R. Soc. London Ser. A* **201**, 192 (1950).
4. J. D. Lindl and W. C. Mead, *Phys. Rev. Lett.* **34**, 1273 (1975).
5. V. N. Goncharov, J. P. Knauer, P. W. McKenty, P. B. Radha, T. C. Sangster, S. Skupsky, R. Betti, R. L. McCrory, and D. D. Meyerhofer, *Phys. Plasmas* **10**, 1906 (2003).
6. S. E. Bodner, *Phys. Rev. Lett.* **33**, 761 (1974).
7. H. Takabe *et al.*, *Phys. Fluids* **28**, 3676 (1985).
8. R. Betti, V. N. Goncharov, R. L. McCrory, P. Sorotkin, and C. P. Verdon, *Phys. Plasmas* **3**, 2122 (1996).
9. Laboratory for Laser Energetics LLE Review **94**, 91, NTIS document No. DOE/SF/19460-485 (2003). Copies may be obtained from the National Technical Information Service, Springfield, VA 22161.
10. T. J. B. Collins and S. Skupsky, *Phys. Plasmas* **9**, 275 (2002).
11. S. E. Bodner, *J. Fusion Energy* **1**, 221 (1981).
12. S. Skupsky, R. W. Short, T. Kessler, R. S. Craxton, S. Letzring, and J. M. Soures, *J. Appl. Phys.* **66**, 3456 (1989).
13. T. R. Boehly, D. L. Brown, R. S. Craxton, R. L. Keck, J. P. Knauer, J. H. Kelly, T. J. Kessler, S. A. Kumpan, S. J. Loucks, S. A. Letzring, F. J. Marshall, R. L. McCrory, S. F. B. Morse, W. Seka, J. M. Soures, and C. P. Verdon, *Opt. Commun.* **133**, 495 (1997).
14. J. P. Knauer, R. Betti, D. K. Bradley, T. R. Boehly, T. J. B. Collins, V. N. Goncharov, P. W. McKenty, D. D. Meyerhofer, V. A. Smalyuk, C. P. Verdon, S. G. Glendinning, D. H. Kalantar, and R. G. Watt, *Phys. Plasmas* **7**, 338 (2000).
15. M. C. Richardson, P. W. McKenty, F. J. Marshall, C. P. Verdon, J. M. Soures, R. L. McCrory, O. Barnouin, R. S. Craxton, J. Delettrez, R. L. Hutchison, P. A. Jaanimagi, R. Keck, T. Kessler, H. Kim, S. A. Letzring, D. M. Roback, W. Seka, S. Skupsky, B. Yaakobi, S. M. Lane, and S. Prussin, in *Laser Interaction and Related Plasma Phenomena*, edited by H. Hora and G. H. Miley (Plenum Publishing, New York, 1986), Vol. 7, pp. 421–448.
16. O. L. Landen *et al.*, in *Ultrahigh- and High-Speed Photography, Videography, and Photonics '93*, edited by P. W. Roehrenbeck (SPIE, Bellingham, WA, 1993), Vol. 2002, pp. 2–13.
17. Y. Lin, T. J. Kessler, and G. N. Lawrence, *Opt. Lett.* **20**, 764 (1995).
18. T. R. Boehly, V. A. Smalyuk, D. D. Meyerhofer, J. P. Knauer, D. K. Bradley, R. S. Craxton, M. J. Guardalben, S. Skupsky, and T. J. Kessler, *J. Appl. Phys.* **85**, 3444 (1999).
19. P. B. Radha, V. N. Goncharov, T. J. B. Collins, J. A. Delettrez, P. W. McKenty, and R. P. J. Town, “Two-Dimensional Simulations of Plastic-Shell Implosions on the OMEGA Laser,” to be submitted to *Physics of Plasmas*.